remote sensing

MDPI

Article

A Snow Depth Downscaling Algorithm Based on Deep Learning Fusion of Enhanced Passive Microwave and Cloud-Free Optical Remote Sensing Data in China

Zisheng Zhao [1], Xiaohua Hao [1,2,*], Donghang Shao [1,2], Wenzheng Ji [1,3], Tianwen Feng [4], Qin Zhao [1,3], Wenxin He [5], Liyun Dai [1,2], Zhaojun Zheng [6,7] and Yan Liu [8,9]

1 Key Laboratory of Cryospheric Science and Frozen Soil Engineering, Northwest Institute of Eco-Environment and Resources, Chinese Academy of Sciences, Lanzhou 730000, China; zhaozisheng@nieer.ac.cn (Z.Z.)
2 Heihe Remote Sensing Experimental Research Station, Northwest Institute of Eco-Environment and Resources, Lanzhou 730000, China
3 University of Chinese Academy of Sciences, Beijing 100049, China
4 Faculty of Geomatics, Lanzhou Jiaotong University, Lanzhou 730070, China
5 College of Geographical Sciences, Qinghai Normal University, Xining 810016, China
6 National Satellite Meteorological Center, China Meteorological Administration, Beijing 100081, China
7 Key Laboratory of Radiometric Calibration and Validation for Environmental Satellites, China Meteorological Administration, Beijing 100081, China
8 Institute of Desert Meteorology, China Meteorological Administration, Urumqi 830002, China
9 Xinjiang Taklamakan Desert Meteorological National Field Scientific Observation and Research Station, Urumqi 830002, China
* Correspondence: haoxh@lzb.ac.cn

Abstract: High spatial resolution snow depth (SD) is crucial for hydrological, ecological, and disaster research. However, passive microwave SD product (10/25 km) is increasingly insufficient to meet contemporary requirements due to its coarse spatial resolution, particularly in heterogeneous alpine areas. In this study, we develop a superior SD downscaling algorithm based on the FT-Transformer (Feature Tokenizer + Transformer) model, termed FTSD. This algorithm fuses the latest calibrated enhanced resolution brightness temperature (CETB) (3.125/6.25 km) with daily cloud-free optical snow data (500 m), including snow cover fraction (SCF) and snow cover days (SCD). Developed and evaluated using 42,692 ground measurements across China from 2000 to 2020, FTSD demonstrated notable improvements in accuracy and spatial resolution of SD retrieval. Specifically, the RMSE of temporal and spatiotemporal independent validation for FTSD is 7.64 cm and 9.74 cm, respectively, indicating reliable generalizability and stability. Compared with the long-term series of SD in China (25 km, RMSE = 10.77 cm), FTSD (500 m, RMSE = 7.67 cm) provides superior accuracy, especially improved by 48% for deep snow (> 40 cm). Moreover, with the higher spatial resolution, FTSD effectively captures the SD's spatial heterogeneity in the mountainous regions of China. When compared with downscaling algorithms utilizing the raw TB data and the traditional random forest model, the CETB data and FT-Transformer model optimize the RMSE by 10.08% and 4.84%, respectively, which demonstrates the superiority of FTSD regarding data sources and regression methods. Collectively, these results demonstrate that the innovative FTSD algorithm exhibits reliable performance for SD downscaling and has the potential to provide a robust data foundation for meteorological and environmental research.

Keywords: snow depth; downscaling; deep learning; enhanced spatial resolution

check for updates

Citation: Zhao, Z.; Hao, X.; Shao, D.; Ji, W.; Feng, T.; Zhao, Q.; He, W.; Dai, L.; Zheng, Z.; Liu, Y. A Snow Depth Downscaling Algorithm Based on Deep Learning Fusion of Enhanced Passive Microwave and Cloud-Free Optical Remote Sensing Data in China. *Remote Sens.* **2024**, *16*, 4756. https://doi.org/10.3390/rs16244756

Academic Editor: Peter Romanov

Received: 19 October 2024
Revised: 16 December 2024
Accepted: 18 December 2024
Published: 20 December 2024

Copyright: © 2024 by the authors. Licensee MDPI, Basel, Switzerland. This article is an open access article distributed under the terms and conditions of the Creative Commons Attribution (CC BY) license (https://creativecommons.org/licenses/by/4.0/).

1. Introduction

Snow represents a critical component of the global hydrological cycle and climate system [1], essential to the energy budget and radiative balance between the Earth's surface and atmosphere [2,3]. Snow water equivalent (SWE) is the amount of water contained in completely melted snow and represents the water resources stored in snow, which is critical

for hydrologic modeling and the operation of the climate system [4]. Snowmelt is also the main source of freshwater in arid and semi-arid regions, benefiting about 17% of the global population [5–7]. In China, the average annual snow cover is 11.3%, rising to 27% in winter, and is mainly distributed in the cold or semi-arid regions of the Qinghai–Tibetan Plateau (QTP), northern Xinjiang (NXJ), and northeast China (NEC) [8,9], where snow is relevant for agricultural development and water supply security. Snow depth (SD) is a crucial parameter for snow, and monitoring its spatial and temporal dynamics is essential for quantifying SWE, managing water resources, and mitigating disasters [4,10].

However, most snow is located in remote mountainous regions, and field observations do not adequately represent long-term and large-scale changes in SD, so satellite remote sensing monitoring is an effective method to monitor SD, primarily through active microwave and passive microwave [4]. Among them, active microwave features high spatial resolution, and its phase and intensity information have shown significant potential in high precision and high spatial resolution SD mapping [11,12]. However, the current active microwave satellite data face challenges in covering large areas and achieving frequent revisit time, making it difficult to monitor large regions continuously.

Passive microwave (PMW) brightness temperature (TB) has provided daily global records since 1978, making it a key data source for estimating SD at global and regional scales [1,13]. In the early work, Chang et al. [14] analyzed the differences in volumetric scattering effects of snow under dry conditions and established an empirical relationship between the brightness temperature difference (TBD) at 18 GHz and 36 GHz with SD. Subsequently, several researchers have enhanced the applicability of the empirical relationship by integrating influencing factors, including forest cover [15–17], land cover type (LC) [18], and temperature gradient index (TGI) [19]. However, the attenuation of microwave radiation energy caused by volume scattering is not only related to SD but also influenced by complex properties such as underlying surface, density, and grain size. The empirical relationship has considerable uncertainty in different temporal and spatial conditions [1,20,21]. Existing microwave radiation models have been used to estimate SD by quantifying snow parameters [21,22], which often require complex and variable parameters (such as snow and soil), posing substantial challenges to universal applicability [13,23]. Consequently, deriving SD solely from PMW data through simple empirical relationships or rigorous physical model approaches is problematic, and it is difficult to effectively capture the fine spatial distribution, especially in mountainous areas [10,24].

Since optical remote sensing features a higher spatial resolution, monitoring spatiotemporal dynamic snow is effective. To enhance the spatial resolution of PMW SD retrieval, the integration of optical remote sensing data for snow identification is a practical approach, which specifically includes snow cover extent (SCE) [25], snow cover fraction (SCF) [24,26], and snow phenology parameter snow cover days (SCD) [8,27]. SCE and SCF perform downscaling by describing the spatial distribution ratio of snow within PMW coarse resolution pixels. The binary snow distribution of SCE encounters significant challenges in complex terrains and patchy snow [28,29]. SCF offers more accurate subpixel scale information on snow [30,31], making it more suitable for providing spatial heterogeneity insights. SCD is utilized to improve the spatial resolution of SD based on its fraction within coarse resolution pixels. However, preexisting SD is generally the subject of downscaling in these studies, typically derived from coarse resolution TB data through empirical linear methods. These methods fit relationships that are too simple to align with the spatial and temporal heterogeneity of snow, retaining inherent uncertainties in the final downscaling results.

With the development of machine learning (ML) and deep learning (DL), their ability to address nonlinear relationships among multiple features presents substantial potential for SD downscaling. Recent studies have utilized this capability to integrate TB, specific optical snow information (SCE, SCF, or SCD), and terrain attributes for SD downscaling, achieving accuracy and spatial resolution optimization [32,33]. Despite ML and DL having advantages over linear empirical fitting, the regression models used in these studies are still traditional methods (random forest and simple neural network), which have not kept pace

with the rapid development of DL. Many advanced DL architectures, like the Transformer backbone [34], are well suited to capturing complex nonlinear relationships and have been used in vision, language, and other frontier applications [35,36]. Additionally, these studies have not fully integrated the downscaling effectiveness of SCF and SCD. Optical remote sensing is influenced by clouds, and there have been notable developments in reconstructing snow information under clouds [37,38], but it lacks timely application. Furthermore, there is a notable difference in spatial resolution between PMW TB data (10/25 km) and optical snow cover information (500 m). Recently, Brodzik et al. [39] developed the calibrated enhanced resolution brightness temperature (CETB), which achieves the highest spatial resolution of 3.125 km with an image reconstruction technique, demonstrating substantial spatial advantages in the study of sea ice [40], lake ice [41], and snow [42,43]. As such, based on the current advancement of DL, the full integration of CETB and cloud-free snow products presents notable potential for improving SD downscaling.

Consequently, there remains considerable scope for optimizing the current SD downscaling algorithm regarding the data sources and retrieval methods. To address these limitations, this study develops an SD downscaling algorithm based on the DL deep model FT-Transformer (Feature Tokenizer + Transformer), termed FTSD, which integrates the latest CETB and cloud-free optical snow data. This algorithm was developed and evaluated using ground measured SD in China from 2000 to 2020, followed by a comparative analysis with the widely applied 25 km long-term SD dataset in China in terms of accuracy and spatial distribution. Furthermore, this study explores the advantages of the algorithm regarding TB sources and regression models, alongside the impact of various error factors on its performance.

2. Data and Preprocessing

2.1. Enhanced Resolution PMW Data

This study designates the annual snow season (October to April) from 2000 to 2020 as the research period. The CETB data (https://nsidc.org/data/NSIDC-0630/versions/1, accessed on 20 March 2024) are employed as the basic data for SD retrieval. This dataset utilizes the radiometer version of the Scatterometer Image Reconstruction (rSIR) algorithm to enhance the spatial resolution of raw TB data. The spatial resolutions of commonly used bands at 19 GHz and 37 GHz are improved to 6.25 km and 3.125 km, respectively [43,44]. CETB spans various radiometers since 1987, including SMMR, SSM/I, SSMIS, and AMSR-E. SSM/I and SSMIS are sourced from the DMSP satellite series and are cross-sensor calibrated for continuous studies [39,45]. Considering the temporal continuity of the data throughout the study period, data from the SSM/I (DMSP-F13) and SSMIS (DMSP-F16) sensors are utilized for 2000–2008 and 2009–2020, respectively, including both the vertical polarization and horizontal polarization TB at frequencies of 19.35 GHz and 37 GHz (hereinafter referred to as TB_{19V}, TB_{19H}, TB_{37V}, and TB_{37H}). To reduce the impact of wet snow, only descending data from each sensor are included in this study [46].

2.2. High Spatial Resolution Data

SCF is a downscaling feature that enhances the spatial resolution of SD retrieval by providing fine snow distribution, which reduces the influence of mixed pixels [24]. This study adopted the daily cloud-free SSEmod-SCF data with a resolution of 500 m, derived from an automatic spatial-spectral-environmental feature endmember extraction technique and the linear spectral mixture analysis model (LSMA) [30,37]. The spatio-temporal fusion spatial (STFS) method is employed to fill missing data under cloud, which comprises two steps: a joint cloud removal algorithm in the space and time domains, and cloud removal in the space domain [37]. The RMSE of SCF before cloud removal reaches 0.136, and the overall accuracy of cloud removal is 82.62%, which achieves accurate snow identification and reconstruction of snow information under cloud [30,37].

SCD reflects the long-term accumulation patterns of snow, incorporating the effects of environmental factors such as temperature, precipitation, and topography [9]. It is

an important downscaling feature that provides geographical variation information for SD downscaling [27,33,47]. The SCD data are sourced from the National Cryosphere Desert Data Center (http://www.ncdc.ac.cn, accessed on 1 October 2023), containing China's annual 500 m spatial resolution SCD data from 2000 to 2020 [48]. To facilitate the timely estimation of SD in future applications of the algorithm and obtain more robust environmental accumulation effects in the snow region, this study further generated a multi-year average SCD.

LC influences the microwave radiation signal observed by satellites and can provide information on the heterogeneity of the snow subsurface for optimizing SD retrieval [4,18]. LC is derived from the MCD12Q1 V061 dataset with a spatial resolution of 500 m (https://search.earthdata.nasa.gov). This dataset provides global annual land cover types based on the IGBP classification. This study focuses on the following four types based on the complexity of vegetative cover: water, forest, grassland, and bare land [47].

DEM plays a critical role in snow accumulation, ablation, and transport processes [49], particularly in mountainous regions where the complex topography interferes with microwave radiation transmission processes [50]. The DEM data in this study are derived from the SRTM V4 dataset at a spatial resolution of 90 m (https://srtm.csi.cgiar.org, accessed on 12 June 2023), which provides elevation information for SD retrieval.

2.3. ERA5-Land Data

The internal physical parameters of snow (such as grain size) can affect the response relationship between microwave radiation and the snow layer, impacting SD retrieval [14,51,52]. However, temporally continuous grain size information is not available at large scale. For this reason, we use the temperature gradient (TG) as an indirect indicator of changes in snow grain size [19,52]. The TG is defined as the difference between soil temperature (T_{soil}) and air temperature (T_{air}), where the T_{soil} and T_{air} are sourced from the ERA5-land reanalysis data with a spatial resolution of 10 km (https://cds.climate.copernicus.eu, accessed on 23 June 2023).

2.4. Ground Measurement SD

Ground measurement SD data are obtained from ground measurement stations and field snow courses in China (Figure 1):

(1) Ground measurement stations. The dataset provides the basis for the construction and evaluation of the algorithm and mainly includes measurement data of meteorological stations of the China Meteorological Administration. Based on the spatial representativeness assessment grade of the meteorological stations, which considers the terrain, snow cover, and other conditions around stations [53]. We selected the stations with excellent representativeness in grades 1–3. Additionally, measurements from stations in the Manas River Basin and the Koktokay region from 2011 to 2020 in northern Xinjiang are included.

(2) Field snow courses, supported by the China snow survey project [54], provide a spatiotemporally independent validation subset for the algorithm. During the two snow seasons of 2017–2018 and 2018–2019, the project surveyed two courses in three major snow cover areas: QTP, NXJ, and NEC. Among them, snow courses 1 and 2 in NXJ and snow courses 5 and 6 in NEC are used, but the two courses in QTP with less data and excessive wet snow are excluded.

Since microwave radiation does not exert notable scattering effects in the snow layer below 5 cm [14], we excluded records of measured SD < 5 cm when constructing and evaluating the algorithm. In addition, dry snow was selected from the measured ground measurement using the conditions in Equations (1)–(3) [55] to reduce the effect of wet snow on microwave scattering. In summary, this study used 42,692 ground measurement records, including 42,313 records from 374 stations and 379 records from four field snow courses.

$$15.9 \times (TB_{19V} - TB_{37V}) > 80 \quad (1)$$

$$TB_{37H} < 240 \text{ K} \quad (2)$$

$$TB_{37V} < 250 \text{ K} \quad (3)$$

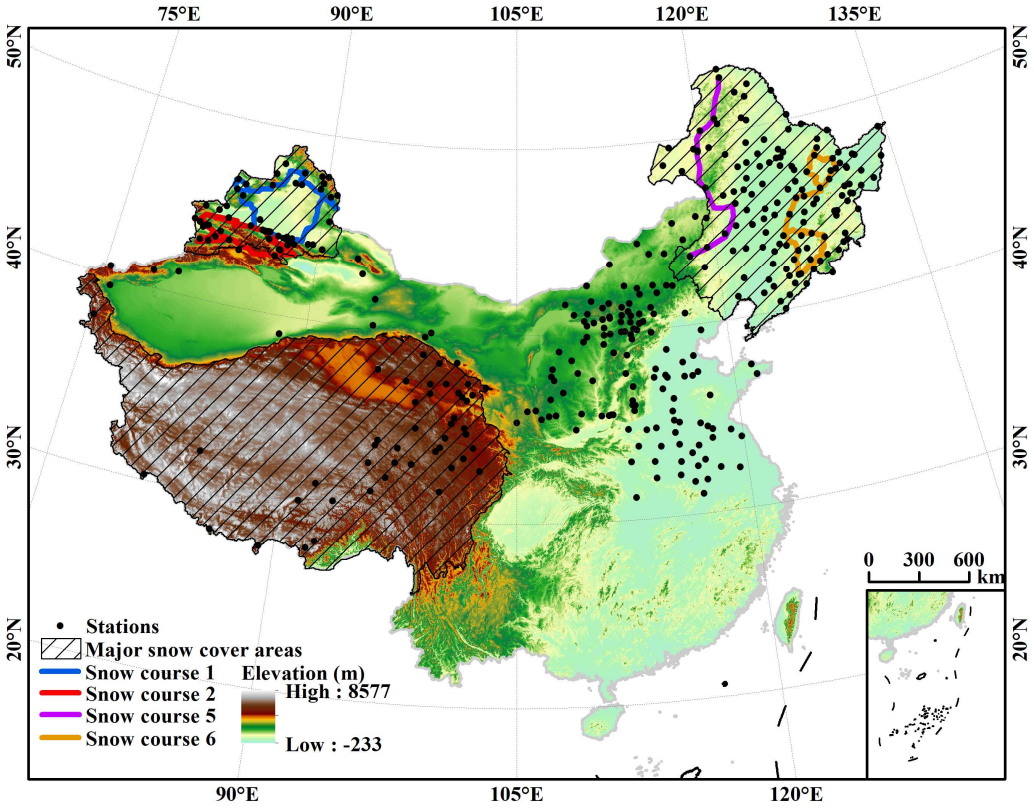


Figure 1. Spatial distribution of ground measurement stations and field snow courses in China.

2.5. Auxiliary Data

To evaluate the capabilities of the SD downscaling algorithm proposed in this study, we acquired a long-term SD dataset for China spanning 2000–2020 (https://data.tpdc.ac.cn, accessed on 23 August 2023). This dataset employs the improved Chang algorithm [14] by Che [15,56], which has been widely applied in analyzing temporal and spatial snow trends [32,57]. The spatial resolution of this dataset is 25 km and is hereinafter referred to as PMSD.

3. Methodology

This chapter focuses on constructing an SD downscaling algorithm based on the FT-Transformer that integrates various features. As shown in Figure 2, the above data sources are used to build FTSD algorithm. The main objective of FTSD construction part is to use the FT-Transformer model to integrate potential features from multiple data sources and then use the ground measurement SD for feature selection and performance evaluation of the algorithm. Consequently, Section 3.1 will introduce the structure and main parameter configurations of FT-Transformer, the deep learning model utilized in this research. Section 3.2 will introduce the construction process of the SD downscaling algorithm FTSD and the potential features of FT-Transformer. Finally, Section 3.3 describes the strategies and metrics to be employed in evaluating algorithmic performance.

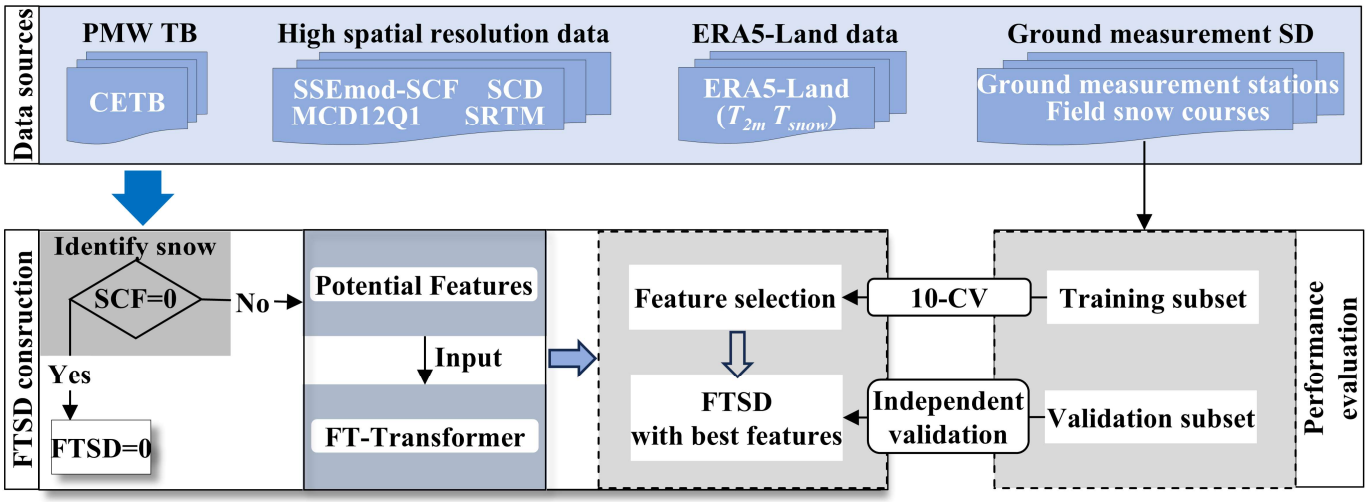


Figure 2. The flowchart of developing the SD downscaling algorithm FTSD in this study, including data sources, construction of FTSD algorithm and its evaluation.

3.1. FT-Transformer Model

This study employed the FT-Transformer (Feature Tokenizer + Transformer) model to map the relationship between features (such as TB) and SD. The FT-Transformer model was adapted by Gorishniy et al. [58] based on the Transformer backbone [34] for application in tabular data, which is capable of learning complex relationships between multiple features with excellent generalization performance. As shown in Figure 3, this model contains three main modules: Feature Tokenizer, Transformer, and Prediction module. The Feature Tokenizer module stacks the input numerical and categorical features into the embedding vector T through linear and categorical embedding approaches, respectively. The Transformer module appends the [CLS] embedding token to T to obtain T_0 [59], which is then transformed into T_L through multiple transformer blocks, establishing a contextual correlation between [CLS] and the numerical and categorical embedding vector T. The Prediction module outputs the prediction results from [CLS] part of T_L through the linear layer. Among them, the Transformer module mainly consists of transformer blocks. A transformer block is primarily composed of a Multi-Head Self-Attention (MHSA) layer, Residual connection (Add) and LayerNorm, and a Feed Forward Network (FNN). Compared to the original Transformer, FT-Transformer has taken optimization in data embedding. The multiple features are converted into tokens in a unified format through Feature Tokenizer, which facilitates the flexible and efficient modeling between different features in the Transformer layer, making [CLS] more effective in aggregating the global information of input features. Therefore, FT-Transformer is suitable for exploring potential relationships between multiple features, especially for SD retrieval that contain multiple continuous numerical features.

The main configurations of the FT-Transformer model are set as follows: the number of transformer block is 3, the dimension of the MHSA feature embedding is 32, and the number of attention heads is 8. The MHSA and FNN adopt the dropout regularization to improve generalization capacity, with dropout rates of 0.1 and 0.05, respectively. The activation of FNN is ReGLU; the activation of the Prediction module is ReLU. Model training uses the stable and efficient Lamb optimizer [60], and the loss function is the mean squared error (MSE), which is commonly used in regression tasks. Furthermore, to enhance the stability and convergence efficiency of FT-Transformer, the Cosine Annealing Learning Rate (CosineAnnealingLR) [61] is implemented to dynamically adjust the learning rate while incorporating L2 regularization terms for weight decay during optimizer updates of the model parameters.

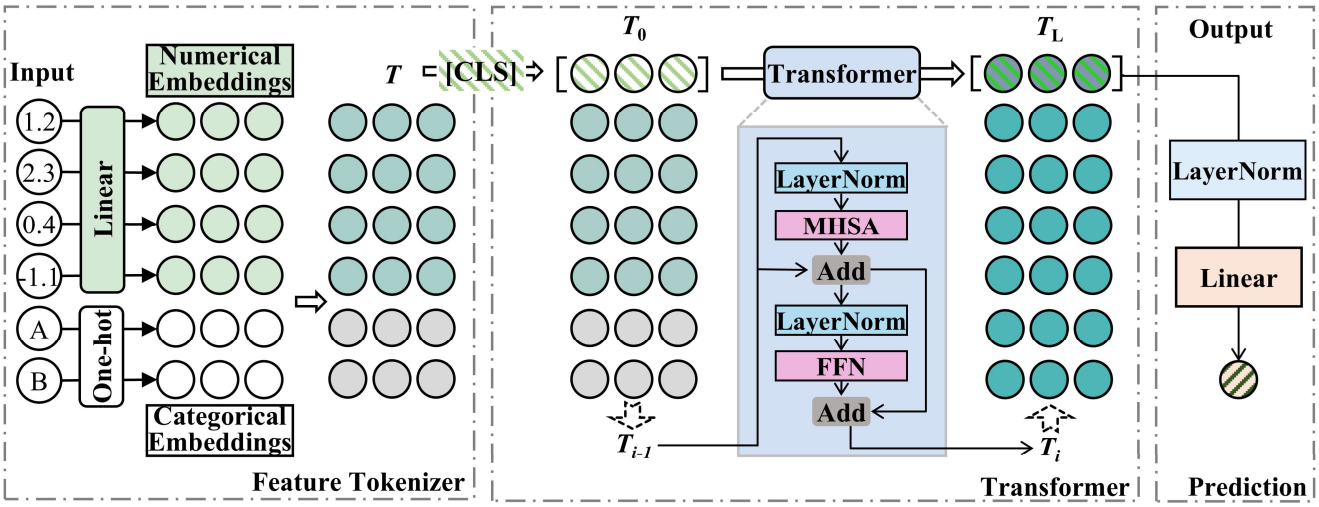


Figure 3. Composition of the FT-Transformer (Feature Tokenizer + Transformer) model, including three main modules: Feature Tokenizer, Transformer, and Prediction.

3.2. SD Downscaling Algorithm

The kilometer-level spatial resolution of PMW data is susceptible to interference from non-snow information in mixed pixels, posing challenges in accurately describing the snow radiation on complex terrains [4,24]. As shown in Figure 2, this study uses cloud-free, high spatial resolution, and high-precision SCF [30,37] as priors to infer snow cover information and divides the construction of FTSD algorithm into two parts. First, when the SCF is 0, it is deemed that there is no snow in the pixel, and the estimated SD is set to 0. When the SCF is greater than 0, it indicates that the pixel is covered by snow. The deep learning model FT-Transformer is utilized to map the intricate nonlinear relationship between potential input features (Table 1) and measured SD for retrieval. To verify the effectiveness of these potential features and select the optimal input features for FTSD, the strategy of gradually adding features is used to compare different feature combinations.

Table 1. Potential input features for SD retrieval by FT-Transformer when SCF > 0.

Features	Contributions
TB (TB_{19V}, TB_{19H}, TB_{37V}, TB_{37H})	Microwave radiation information of snow scattering
TG ($T_{soil} - T_{air}$)	Indirect representation of snow grain size change
LC	Information of the snow underlying surface
DEM	Terrain conditions under snow
SCF	Fine information of snow distribution
SCD	Long-term effects of geographical environment

3.3. Performance Evaluation

To reduce the risk of overfitting and assess the algorithm's generalization performance, we divided the ground measurement data into a training subset and a validation subset (Table 2) during the construction and evaluation of the FTSD algorithm. Ground measurement station data from 2006 to 2016 were used as the training subset to assess the algorithm accuracy via 10-fold cross-validation (10-CV), which was mainly used to select the optimal input features of the algorithm. The data from 2000 to 2006 and 2016 to 2020 were used as the temporally independent validation subset, and field snow courses were used as the spatiotemporally independent validation subset, mainly for performance evaluation of the algorithm after construction.

Table 2. Training and validation subset partitioning of ground measurement data.

Subsets		Ground Measurement Stations	Field Snow Courses
Training	Snow seasons	2006–2015	/
	Samples	16,743	/
	Purpose	10-CV	/
Validation	Snow seasons	2000–2005 and 2016–2020	2017–2019
	Samples	25,570	379
	Purpose	Temporal independent	Spatiotemporal independent

Algorithm accuracy was specifically evaluated using several metrics, including the mean absolute error (MAE), root mean square error (RMSE), and Pearson correlation coefficient (R):

$$\mathrm{MAE} = \frac{\sum_{i=1}^{n} |x_i - y_i|}{n} \tag{4}$$

$$\mathrm{RMSE} = \sqrt{\frac{\sum_{i=1}^{n} (x_i - y_i)^2}{n}} \tag{5}$$

$$\mathrm{R} = \frac{\sum_{i=1}^{n} (x_i - \overline{x})(y_i - \overline{y})}{\sqrt{\sum_{i=1}^{n} (x_i - \overline{x})^2} \sqrt{\sum_{i=1}^{n} (y_i - \overline{y})^2}} \tag{6}$$

where n is the number of samples with measured SD, x_i is the measured SD, y_i is the SD calculated by the FTSD algorithm, $\overline{x}$ is the mean x_i, and $\overline{y}$ is the mean y_i.

4. Results

4.1. Selection of the Input Features

The performance of FTSD under different features is evaluated using the Training subset. As depicted in Table 3, these potential features can provide valuable information from different perspectives for SD downscaling. After considering a comprehensive array of features, the FTSD demonstrates superior effectiveness, with MAE, RMSE, and R at 4.46 cm, 6.64 cm, and 0.83, respectively. Consequently, TB, TG, LC, DEM, SCF, and SCD are identified as the FTSD's input features in the downscaling for SD retrieval. In particular, when SCF and SCD are progressively added, the RMSE gradually increases by 5.76% and 5.55%, which shows the necessity of fully integrating SCF and SCD features.

Table 3. The 10-CV accuracy of FTSD with different input feature combinations.

Input Feature Combinations	MAE (cm)	RMSE (cm)	R
TB	6.81	9.59	0.58
TB + TG	6.25	9.00	0.64
TB + TG + LC	5.90	8.54	0.69
TB + TG + LC + DEM	5.08	7.46	0.77
TB + TG + LC + DEM + SCF	4.96	7.03	0.80
TB + TG + LC + DEM + SCF + SCD	**4.46**	**6.64**	**0.83**

4.2. Algorithm Performance Evaluation

4.2.1. Accuracy Evaluation of Temporally and Spatiotemporally Independent

Figure 4 shows the accuracy of FTSD on independent validation subsets in Table 2. FTSD exhibits commendable temporally independent accuracy, with MAE at 5.34 cm, RMSE at 7.64 cm, and R at 0.73, as shown in Figure 4a. These results suggest that FTSD effectively predicts the SD for periods beyond the training subset, demonstrating superior temporal generalization performance. As illustrated in Figure 4b, the spatiotemporal independent accuracy of FTSD is relatively low, with MAE at 6.61 cm, RMSE at 9.74 cm, and R at

0.59, indicating that the pronounced spatial heterogeneity of snow has a considerable influence on SD estimation. Snow course 2 shows a relatively high retrieval error, with notable underestimation when measured SD exceeds 40 cm, which is consistent with the verification bias shown in Figure 4a. It is important to note that snow course 2 is located near the topographically complex region of the Tianshan Mountains in NJ (Figure 1), where the ground measurement records indicate deeper SD.

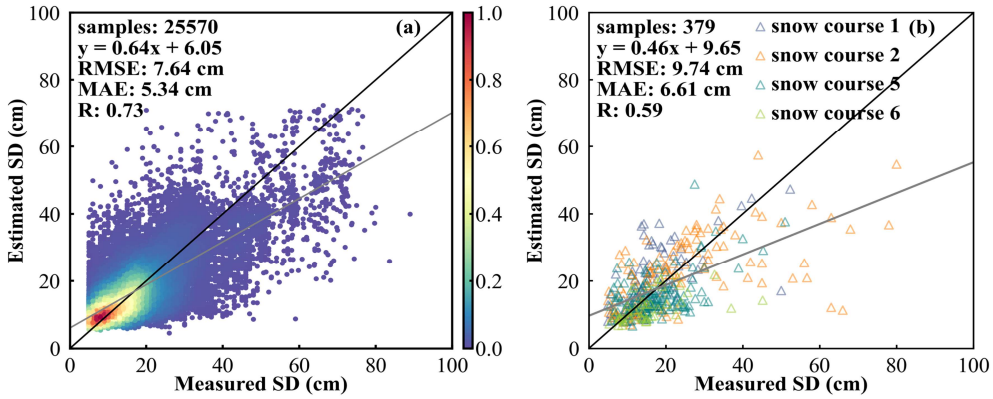


Figure 4. Accuracy of FTSD on the independent validation subsets. (**a**) Temporally independent validation density scatterplots based on ground measurement stations, the color bar is the relative distribution density of scatter plots after normalization by Gaussian kernel density estimation; (**b**) Spatiotemporally independent validation scatterplots based on field snow courses.

4.2.2. Stability Assessment in Temporal and Spatial Dimensions

To evaluate the temporal stability of FTSD, the RMSE of ground measuring stations on different snow cover dates during the snow season are counted, including the average SD (Figure 5). The results show that the performance of FTSD is stable during the snow season, with monthly average RMSE of less than 10 cm and daily RMSE generally less than 14 cm. Especially in the snow stability stage (December to January), the interquartile of FTSD is less than 4 cm, and the estimated value is very close to the measured value. It can be found that even in the snow melt stage (March to April), the average measured SD is gradually increasing, which is attributed to the dry snow filtering process in Section 2.4, which removes some wet snow records in the snow melt stage and retains more deep snow records in cold areas. Correspondingly, the RMSE of FTSD is higher in this stage, with an interquartile value above 6 cm.

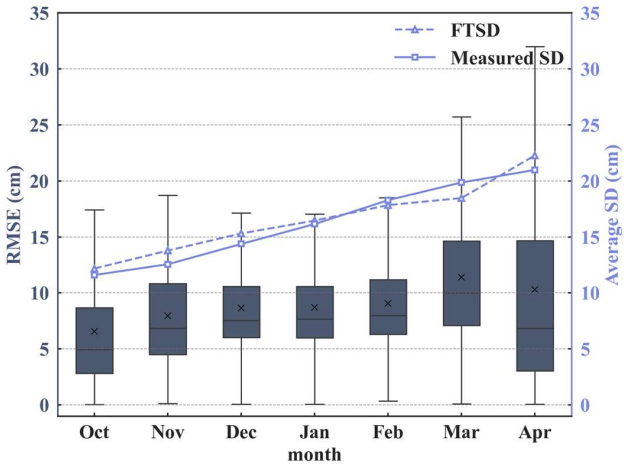


Figure 5. The box plot is a monthly display of the FTSD's RMSE across different snow cover dates at ground measurement stations during the snow season, and the line represents the average of FTSD and measured SD for different months.

To evaluate the spatial stability of FTSD across different geographical regions, this part calculates the RMSE of different ground measurement stations in the main snow cover areas NJ, QTP, and NEC, including the corresponding average SD (Figures 6 and 7). The results show that FTSD performs reliably at most stations, and the estimated value is always consistent with the measured value, exhibiting reliable spatial stability. However, the performance of FTSD varies across different snow cover areas, with larger errors in NJ and better accuracy in QTP, which is generally consistent with the relative size of average SD in these areas.

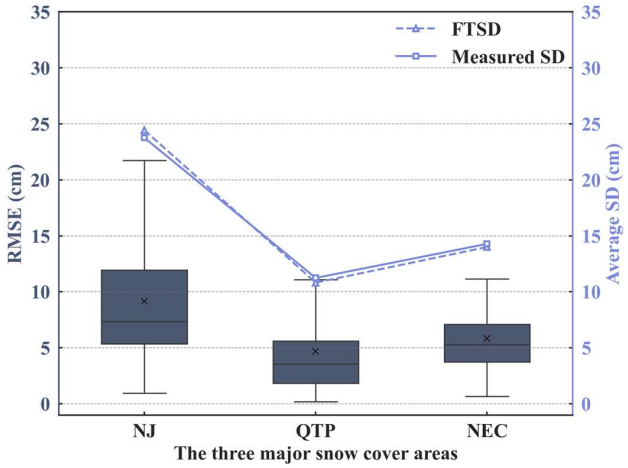


Figure 6. RMSE across different ground measurement stations of the FTSD within the three major snow cover areas (NJ, QTP, and NEC, where the line represents the average SD of FTSD and measured values for different areas.

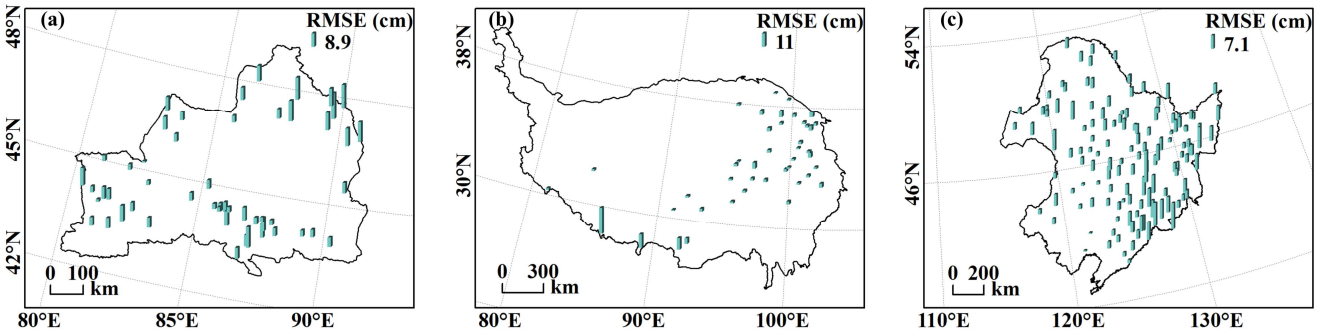


Figure 7. Spatial distribution of the FTSD's RMSE across different ground measurement stations within the three major snow cover areas. (**a**) NJ; (**b**) QTP; (**c**) NEC.

4.3. Comparison of FTSD and the Existing PMSD

The validation subset in Table 2 was used to compare the accuracy difference between FTSD and existing PMSD (Figure 8). The results show that the MAE, RMSE, and R of FTSD are 5.36 cm, 7.67 cm, and 0.73, respectively (Figure 8a), and the overall accuracy is better than that of PMSD, which is 7.37 cm, 10.77 cm, and 0.48 (Figure 8b). It is important to note that the validation subset does not include shallow snow (<5 cm). However, there are many values below 5 cm (including 0) in the PMSD, while there are almost none in FTSD. According to 2,138,309 ground measurement records including the case of SCF = 0, it is found that the correct proportion of FTSD and PMSD in identifying the presence or absence of snow (whether the reversed SD is greater than 0) is 95.43% and 90.72%, respectively. This demonstrates that FTSD, which integrates high spatial resolution optical data, effectively reduces the error of snow identification. Furthermore, Figure 8 reveals that FTSD and PMSD exhibit similar estimation biases, both overestimating shallow snow and underestimating deep snow. To quantify the performance differences of the algorithms

at various SD, we analyzed the retrieval performance of FTSD and PMSD under different SD. As shown in Figure 9, the RMSE of the two estimations increases with the measured SD, while FTSD consistently outperforms PMSD. Notably, under deep snow conditions (> 40 cm), FTSD's accuracy improves by 48%.

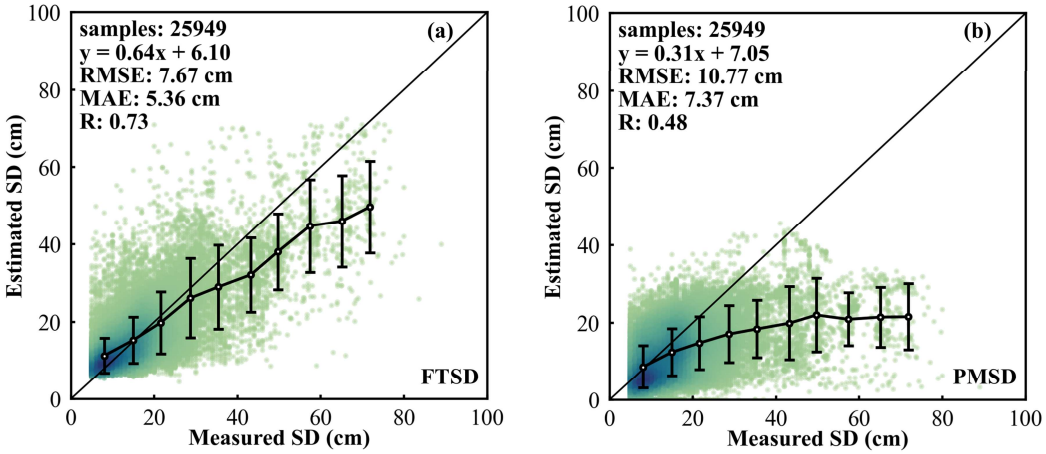


Figure 8. Scatterplot of retrieval accuracy for (**a**) FTSD and (**b**) PMSD on the validation subsets.

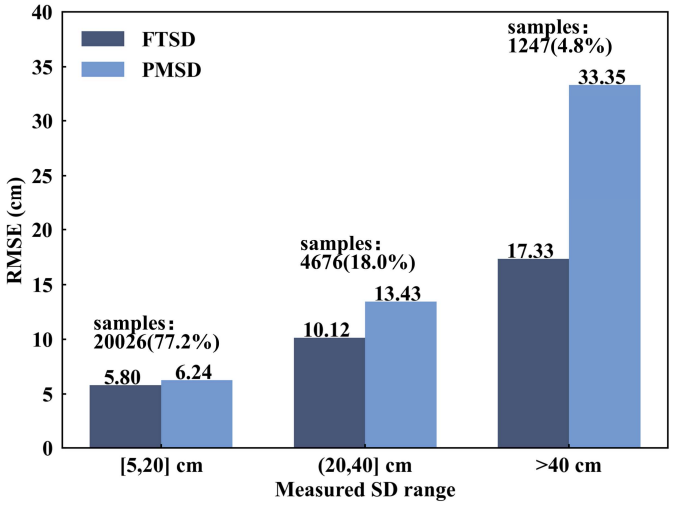


Figure 9. Comparison of the RMSE between FTSD and PMSD at different measured SD ranges, including the [5, 20] cm, (20,40] cm, and > 40 cm ranges.

Figure 10 shows the spatial distribution of FTSD and PMSD on 15 January 2019, presented using a uniform symbol system to facilitate the comparison of spatial consistency and difference between them.

In general, the snow cover in China is mainly concentrated in three major snow cover areas, and both FTSD and PMSD reflect this characteristic, while FTSD tends to show a finer distribution (Figure 10a,b). The detailed displays of the three major snow areas in Figure 10c–h indicate that FTSD has consistent distribution characteristics in mountainous areas with the corresponding complex terrain, whereas the coarse-resolution PMSD struggles to describe this strong spatial heterogeneity. As shown in Figure 10c, FTSD clearly shows the deep snow areas in the Tianshan and Altai Mountains in NJ and reflects the patchy distribution of shallow snow in the Tianshan Mountains and adjacent gentle terrains. The QTP is characterized by complex topography and uneven snow distribution [24]. Figure 10e,f shows that FTSD provides more accurate spatial information for QTP, which is consistent with the patchy distribution characteristic. In NEC, the spatial distribution of the two SD is well consistent, with snow cover and deep snow mainly distributed along the Great Khingan, Lesser Khingan, and Changbai Mountains (Figure 10g,h). Additionally,

previous studies have demonstrated that PMSD exhibits an underestimation bias in NJ [57], while FTSD provides a more realistic estimate (Figure 10c,d).

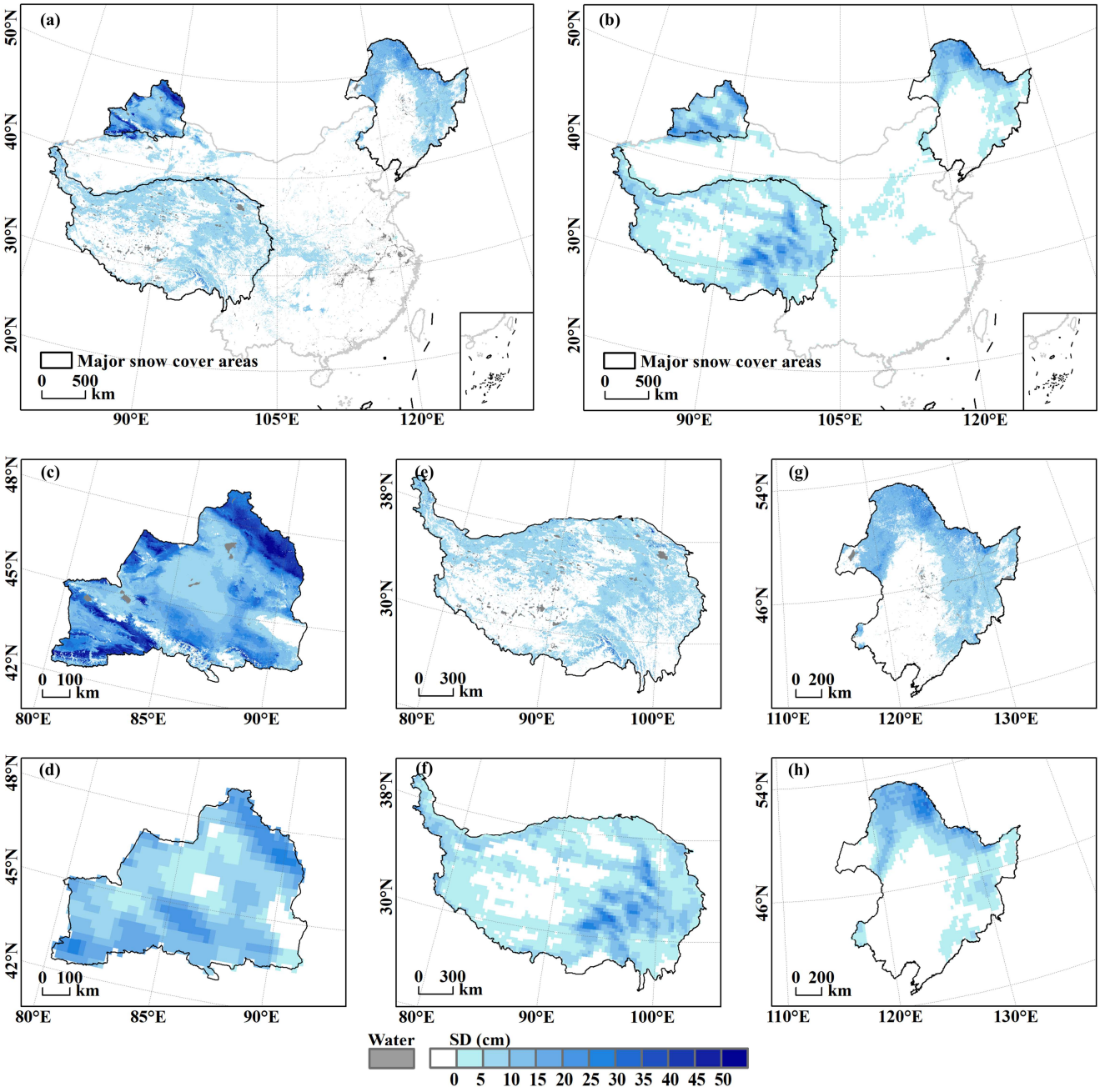


Figure 10. Spatial distribution of FTSD and PMSD on January 15, 2019. (**a**,**c**,**e**,**g**): FTSD distribution for China, NJ, QTP, and NEC, respectively. Data missed due to satellite orbital gaps are interpolated using data from the previous days and the next days; (**b**,**d**,**f**,**h**): PMSD distribution for China, NJ, QTP, and NEC, respectively.

5. Discussion

5.1. Advantages Analysis of the FTSD

Due to limitations in current SD downscaling algorithms regarding data sources and regression methods, this study explores the potential advantages of the proposed FTSD algorithm in addressing these issues. In this section, we employ the raw 25 km resolution TB (RAW TB) and the widely used random forest (RF) model in geosciences to construct three alternative algorithms for comparison with FTSD (Figure 11). The

comparison results show that FTSD has superior SD downscaling potential regarding TB features and regression models, and this advantage is particularly pronounced in deep snow conditions. Specifically, the accuracy performance of RFSD-RAW, FTSD-RAW, RFSD, and FTSD improves sequentially. The RMSE of FTSD is optimized by 4.84% compared to RFSD and by 17.88% under deep snow, indicating that the DL model FT-Transformer is more effective at uncovering relationships between features than the traditional tree model RF. On the other side, FTSD achieves a 10.08% reduction in RMSE compared to FTSD-RAW and a 25.75% improvement under deep snow, indicating that the CETB after image reconstruction can better describe the snow information compared to the RAW TB.

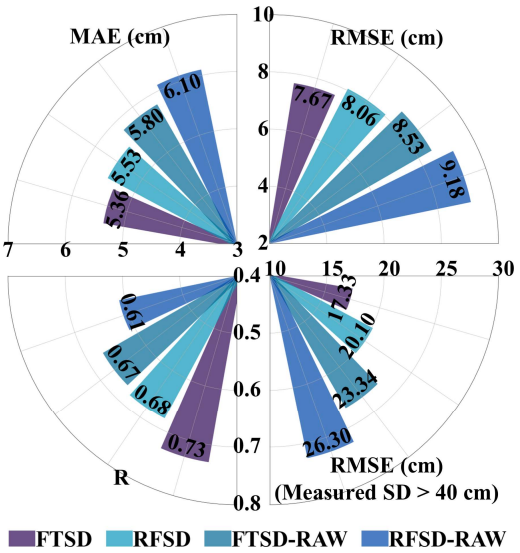


Figure 11. Comparison of the accuracy of FTSD with RFSD, FTSD-RAW, and RFSD-RAW, where FTSD refers to the FT-Transformer + CETB developed in this study, RFSD is RF + CETB, FTSD-RAW is FT-Transformer + RAW TB, and RFSD-RAW is RF + RAW TB. The four sector areas represent the MAE, RMSE, R, and the RMSE in deep snow conditions (>40 cm).

5.2. Error Analysis of Different Factors

Our study shows that the algorithm's performance is different across regions (Figures 6 and 7). In this section, we further discuss the effect of different geographic conditions on the algorithm error, for which the performance of FTSD in different LC, DEM, SCF, and SCD scenes was statistically determined. As shown in Figure 12, the features LC, DEM, SCD, and SCF have varying degrees of influence on algorithm error. It can also be found that FTSD shows reliable applicability across various geographical conditions, with the estimated SD closely matching the measured SD.

Specifically, the results show that FTSD performs best on bare land, has a higher RMSE in grasslands but close to the measured SD, and shows the lowest RMSE in the forest despite considerable underestimation. Theoretically, LC type has a different effect on the radiometric information of snow within a pixel, while bare ground has less of an effect. Although mixed pixels in grasslands affect SD estimation, sufficient measurement data (32%) prompted DL model to further explore the relationship between microwave radiation and SD. In contrast, limited data (1%) in forests made it difficult to obtain reliable mapping relationships and validation results, and the complex vertical structure of forested areas strongly interfered with snow microwave radiation [62,63]. As the elevation increases, the geographic conditions of snow become more complex, and the RMSE increases accordingly until the RMSE exceeds 12 cm at an elevation of more than 2000 m. However, the estimated SD always agrees with the measured values, which indicates the good applicability of the algorithm. Notably, an increase in SCF theoretically reduces the impact of mixed pixels and promotes SD retrieval. However, Figure 12 shows an overall increasing trend in RMSE as SCF increases. This is attributed to the fact that the measured SD increases in step with

the SCF, making retrieval more difficult (Figure 9). When the pixel's SCF is maximized to 100 and is regarded as a pure snow pixel (ignoring the SCF error), the RMSE reaches more than 8 cm, and the average measured SD exceeds 18 cm. Figure 12 shows that different SCD correspond to much different SD, which has an important effect on retrieval. When SCD exceeds 150 days, the average measured SD is close to 30 cm, and there is an underestimation error in the estimation.

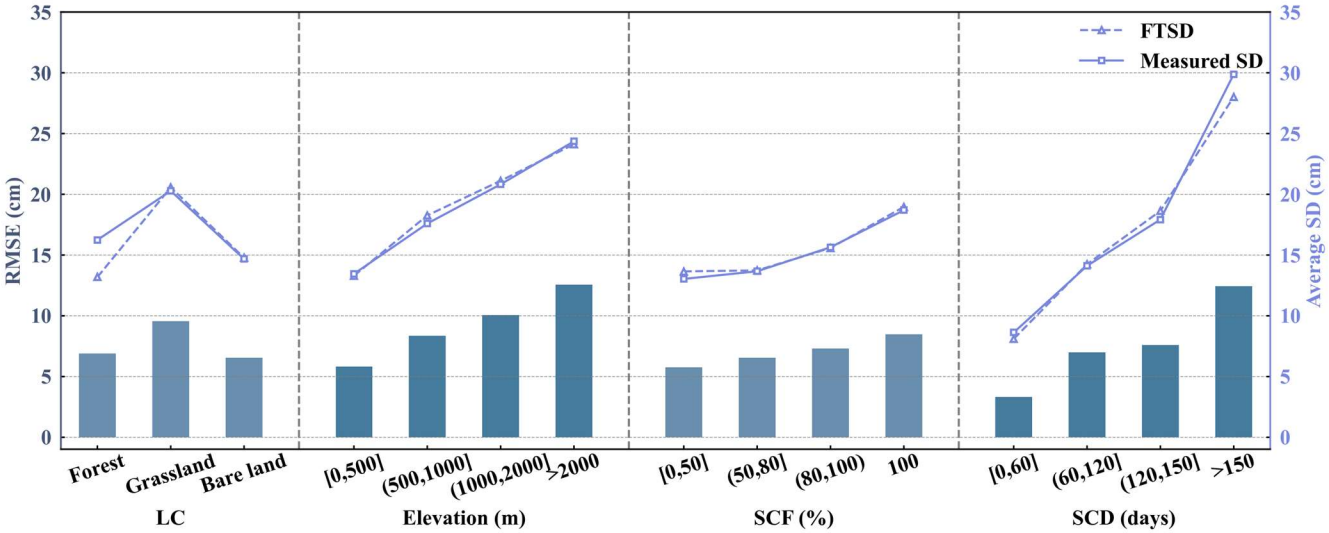


Figure 12. RMSE and average SD of FTSD under different LC, DEM, SCD, and SCF scenes, where the bars represent the RMSE values of FTSD and the lines represent the average SD of FTSD and measured values.

5.3. Advantages and Limitations

The validation analysis of ground measured data indicates that the algorithm FTSD exhibits notable advantages regarding data source and regression model. FTSD achieves high precision in SD retrieval and effectively enhances its spatial resolution, exhibiting reliable temporal and spatial stability, along with the potential for long-term and large-scale application of downscaled SD.

However, this algorithm has some limitations that should be considered. Firstly, although FTSD is more accurate than PMSD in deep snow (>40 cm), the RMSE still reaches a relatively high 17 cm, indicating inadequate performance in estimating deep snow (Figure 9). On the one hand, the quantity of deep snow ground measurements is limited, which leads to the lack of expression ability for deep snow, introducing underestimation bias. In addition, deep snow is mainly located in long-term snow-covered areas in remote mountains, making it difficult to obtain sufficient observations to improve SD retrieval (Figure 12). On the other hand, the penetration capacity of microwave is diminished within deep snow. The specific reason is closely related to the complex internal structure of snow, such as the snow grain size; enhancing the description of the internal structure could improve the ability of PMW to detect deep snow [63,64].

Secondly, the accuracy and stability of the algorithm decrease during the snow melt stage (Figure 5). This is mainly attributed to the impact of wet snow, although some wet snow has been excluded from the measurement data. As the liquid water increases in snow during snow melt stage, the dielectric properties of snow are notably changed. This results in a notable reduction in the volume scattering effect of the snow layer, and instead, it mainly manifests as an emission characteristic, limiting the microwave penetration ability. Consequently, the TB observed by satellite mainly comes from the wet snow surface, making it difficult to estimate SD. From another perspective, the freeze–thaw cycles caused by substantial temperature changes between morning and evening lead to repeated melting and reconstitution of snow grains, further complicating the microwave radiation processes [20,51,63].

Finally, owing to the limited availability of measured SD data in forested regions and the influence of canopy's own radiation and its attenuation effects on snow radiation, FTSD needs to enhance the consideration of radiation process in forest areas and collect more data to optimize the algorithm performance.

6. Conclusions

Accurate high-resolution SD is crucial for water resource monitoring and climate change research. In this study, to address the limitations of existing PMW SD downscaling studies related to data sources and retrieval methods, we developed a novel SD downscaling algorithm, FTSD, fusing the enhanced-resolution PMW and daily cloud-free optical remote sensing data based on the deep learning model FT-Transformer. The FTSD enables the retrieval of the downscaled SD with a spatial resolution of 500 m. The algorithm was constructed and validated using measured SD data during the snow season in China from 2000 to 2020, revealing reliable retrieval accuracy and spatiotemporal applicability from multiple perspectives. The main conclusions are as follows:

(1) The gradual addition of features indicates that multiple features provide effective information for SD retrieval and also proves the necessity of comprehensively considering SCF and SCD. Consequently, the optimal feature combination identified for FTSD includes TB, TG, LC, DEM, SCF, and SCD.

(2) The SD downscaling algorithm FTSD exhibits reliable spatiotemporal generalizability and stability. The downscaled results effectively capture the spatial heterogeneity of SD in mountainous regions. The validation results of temporally independent are 5.34 cm for MAE, 7.64 cm for RMSE, and 0.73 for R, and the spatiotemporally independent accuracies are 6.61 cm, 9.74 cm, and 0.59, respectively. The algorithm also maintains stable accuracy across various snow cover dates and stations, consistent with the measured SD. Compared to the widely applied PMSD (25 km, RMSE = 10.77 cm), the FTSD (500 m, RMSE = 7.67 cm) exhibits superior accuracy, especially in deep snow (RMSE: PMSD = 33.35 cm, FTSD = 17.33 cm). In terms of the spatial distribution of SD, the FTSD reflects significant spatial heterogeneity within mountainous areas from a finer resolution perspective.

(3) The FTSD demonstrates superior potential for SD estimation in both TB sources and regression models. Comparative validation reveals that the FTSD achieves a 10.08% RMSE advantage when utilizing the CETB over RAW TB, whereas the deep learning model FT-Transformer improves RMSE by 4.84% relative to the machine learning model RF. These advantages are particularly pronounced in deep snow, where the optimization is more than 17%.

The FTSD algorithm developed in this study integrates multiple sources of snow information, resulting in high estimation accuracy and strong spatiotemporal stability. Nonetheless, the algorithm lacks considerations for the snow layer structure and microwave radiative transfer process, presenting limitations and challenges. These limitations lead to notable underestimation bias in deep snow conditions and challenges in retrieval during snow melt stage, as well as complex canopy interference in forested areas. To address these challenges and optimize the downscaling for SD retrieval, further research requires the collection of more ground measurement data in deep and forested areas. Furthermore, integrating the microwave radiative transfer model to enhance the characterization of internal structure of snow layer and radiative processes will be a key direction for future research.

Author Contributions: Conceptualization, Z.Z. (Zisheng Zhao) and X.H.; methodology, Z.Z. (Zisheng Zhao) and X.H.; software, Z.Z. (Zisheng Zhao); validation, Z.Z. (Zisheng Zhao) and X.H.; formal analysis, Z.Z. (Zisheng Zhao), X.H. and D.S.; investigation, Z.Z. (Zisheng Zhao), X.H., W.J. and Q.Z.; resources, Z.Z. (Zisheng Zhao), X.H., W.J., Q.Z., L.D., Z.Z. (Zhaojun Zheng) and Y.L.; data curation, Z.Z. (Zisheng Zhao) and X.H.; writing—original draft preparation, Z.Z. (Zisheng Zhao); writing—review and editing, X.H., W.J., D.S. and T.F.; visualization, Z.Z. (Zisheng Zhao) and X.H.;

supervision, T.F. and W.H.; funding acquisition, X.H. and Y.L. All authors have read and agreed to the published version of the manuscript.

Funding: This research was funded by the following projects: the Tianshan Talent Training Program (Grant No. 2023TSYCCX0079), the National Natural Science Foundation of China (Grant No. U22A20564), the Key Project of Natural Science Foundation of Gansu Province (Grant No. 24JRRA082), and the program of the Key Laboratory of Cryospheric Science and Frozen Soil Engineering, CAS (Grant No. CSFSE-ZZ-2402, CSF-SE-ZZ-2409).

Data Availability Statement: The data utilized in this study are detailed in the data section of the article. Further inquiries can be directed to the corresponding author.

Acknowledgments: The authors appreciate all the data provided by each open database. The authors would like to thank the editor and anonymous reviewers for their valuable comments and suggestions on this article.

Conflicts of Interest: The authors declare no conflicts of interest.

References

1. Pulliainen, J.; Luojus, K.; Derksen, C.; Mudryk, L.; Lemmetyinen, J.; Salminen, M.; Ikonen, J.; Takala, M.; Cohen, J.; Smolander, T.; et al. Patterns and trends of Northern Hemisphere snow mass from 1980 to 2018. *Nature* **2020**, *581*, 294–298. [CrossRef] [PubMed]
2. He, C.L.; Liou, K.N.; Takano, Y.; Yang, P.; Qi, L.; Chen, F. Impact of Grain Shape and Multiple Black Carbon Internal Mixing on Snow Albedo: Parameterization and Radiative Effect Analysis. *J. Geophys. Res.-Atmos.* **2018**, *123*, 1253–1268. [CrossRef]
3. Kim, Y.; Kimball, J.S.; Robinson, D.A.; Derksen, C. New satellite climate data records indicate strong coupling between recent frozen season changes and snow cover over high northern latitudes. *Environ. Res. Lett.* **2015**, *10*, 084004. [CrossRef]
4. Shi, J.C.; Xiong, C.; Jiang, L.M. Review of snow water equivalent microwave remote sensing. *Sci. China Earth Sci.* **2016**, *59*, 731–745. [CrossRef]
5. Barnett, T.P.; Adam, J.C.; Lettenmaier, D.P. Potential impacts of a warming climate on water availability in snow-dominated regions. *Nature* **2005**, *438*, 303–309. [CrossRef] [PubMed]
6. Change, I.P.O.C. Climate change 2007: The physical science basis. *Agenda* **2007**, *6*, 333.
7. Bormann, K.J.; Brown, R.D.; Derksen, C.; Painter, T.H. Estimating snow-cover trends from space. *Nat. Clim. Change* **2018**, *8*, 924–928. [CrossRef]
8. Huang, X.; Deng, J.; Ma, X.; Wang, Y.; Feng, Q.; Hao, X.; Liang, T. Spatiotemporal dynamics of snow cover based on multi-source remote sensing data in China. *Cryosphere* **2016**, *10*, 2453–2463. [CrossRef]
9. Zhao, Q.; Hao, X.; Wang, J.; Luo, S.; Shao, D.; Li, H.; Feng, T.; Zhao, H. Snow Cover Phenology Change and Response to Climate in China during 2000–2020. *Remote Sens.* **2022**, *14*, 3936. [CrossRef]
10. Xiaodong, H.; Xubing, L.I.; Changyu, L.; Minqiang, Z.; Jianshun, W. Remote sensing inversion of snow cover extent and snow depth/snow water equivalent on the Qinghai-Tibet Plateau: Advance and challenge. *Glaciol. Geocryol.* **2019**, *41*, 1138–1149.
11. Feng, T.; Hao, X.; Wang, J.; Luo, S.; Huang, G.; Li, H.; Zhao, Q. Applicability of alpine snow depth estimation based on multitemporal UAV-LiDAR data: A case study in the Maxian Mountains, Northwest China. *J. Hydrol.* **2022**, *617*, 129006. [CrossRef]
12. Feng, T.; Huang, C.; Huang, G.; Shao, D.; Hao, X. Estimating snow depth based on dual polarimetric radar index from Sentinel-1 GRD data: A case study in the Scandinavian Mountains. *Int. J. Appl. Earth Obs. Geoinf.* **2024**, *130*, 103873. [CrossRef]
13. Saberi, N.; Kelly, R.; Flemming, M.; Li, Q. Review of snow water equivalent retrieval methods using spaceborne passive microwave radiometry. *Int. J. Remote Sens.* **2020**, *41*, 996–1018. [CrossRef]
14. Chang, A.T.C.; Foster, J.L.; Hall, D.K. Nimbus-7 SMMR Derived Global Snow Cover Parameters. *Ann. Glaciol.* **1987**, *9*, 39–44. [CrossRef]
15. Che, T.; Li, X.; Jin, R.; Armstrong, R.; Zhang, T. Snow depth derived from passive microwave remote-sensing data in China. *Ann. Glaciol.* **2008**, *49*, 145–154. [CrossRef]
16. Kelly, R. The AMSR-E Snow Depth Algorithm: Description and Initial Results. *J. Remote Sens. Soc. Jpn.* **2009**, *29*, 307–317. [CrossRef]
17. Foster, J.L.; Chang, A.T.C.; Hall, D.K. Comparison of snow mass estimates from a prototype passive microwave snow algorithm, a revised algorithm and a snow depth climatology. *Remote Sens. Environ.* **1997**, *62*, 132–142. [CrossRef]
18. Jiang, L.; Wang, P.; Zhang, L.; Yang, H.; Yang, J. Improvement of snow depth retrieval for FY3B-MWRI in China. *Sci. China Earth Sci.* **2014**, *57*, 1278–1292. [CrossRef]
19. Josberger, E.G.; Mognard, N.M. A passive microwave snow depth algorithm with a proxy for snow metamorphism. *Hydrol. Process.* **2002**, *16*, 1557–1568. [CrossRef]
20. Tedesco, M.; Jeyaratnam, J. A New Operational Snow Retrieval Algorithm Applied to Historical AMSR-E Brightness Temperatures. *Remote Sens.* **2016**, *8*, 1037. [CrossRef]

21. Kelly, R.E.; Chang, A.T.; Tsang, L.; Foster, J.L. A prototype AMSR-E global snow area and snow depth algorithm. *IEEE Trans. Geosci. Remote Sens.* **2003**, *41*, 230–242. [CrossRef]
22. Jiang, L.; Shi, J.; Tjuatja, S.; Chen, K.S.; Du, J.; Zhang, L. Estimation of Snow Water Equivalence Using the Polarimetric Scanning Radiometer From the Cold Land Processes Experiments (CLPX03). *IEEE Geosci. Remote Sens. Lett.* **2011**, *8*, 359–363. [CrossRef]
23. Tanniru, S.; Ramsankaran, R. Passive Microwave Remote Sensing of Snow Depth: Techniques, Challenges and Future Directions. *Remote Sens.* **2023**, *15*, 1052. [CrossRef]
24. Dai, L.; Che, T.; Xie, H.; Wu, X. Estimation of Snow Depth over the Qinghai-Tibetan Plateau Based on AMSR-E and MODIS Data. *Remote Sens.* **2018**, *10*, 1989. [CrossRef]
25. Gao, Y.; Xie, H.; Lu, N.; Yao, T.; Liang, T. Toward advanced daily cloud-free snow cover and snow water equivalent products from Terra–Aqua MODIS and Aqua AMSR-E measurements. *J. Hydrol.* **2010**, *385*, 23–35. [CrossRef]
26. Hu, X.; Hao, X.; Wang, J.; Dai, L.; Zhao, H.; Li, H. Snow Depth Downscaling Algorithm based on the Fusion of AMSR2 and MODIS Data: A Case Study in Northern Xinjiang, China. *Remote Sens. Technol. Appl.* **2021**, *36*, 1236–1246.
27. Mhawej, M.; Faour, G.; Fayad, A.; Shaban, A. Towards an enhanced method to map snow cover areas and derive snow-water equivalent in Lebanon. *J. Hydrol.* **2014**, *513*, 274–282. [CrossRef]
28. Parajka, J.; Blöschl, G. Spatio-temporal combination of MODIS images—Potential for snow cover mapping. *Water Resour. Res.* **2008**, *44*. [CrossRef]
29. Czyzowska-Wisniewski, E.H.; van Leeuwen, W.J.D.; Hirschboeck, K.K.; Marsh, S.E.; Wisniewski, W.T. Fractional snow cover estimation in complex alpine-forested environments using an artificial neural network. *Remote Sens. Environ.* **2015**, *156*, 403–417. [CrossRef]
30. Zhao, H.; Hao, X.; Wang, J.; Li, H.; Huang, G.; Shao, D.; Su, B.; Lei, H.; Hu, X. The Spatial–Spectral–Environmental Extraction Endmember Algorithm and Application in the MODIS Fractional Snow Cover Retrieval. *Remote Sens.* **2020**, *12*, 3693. [CrossRef]
31. Zhao, Q.; Hao, X.; Che, T.; Shao, D.; Ji, W.; Luo, S.; Huang, G.; Feng, T.; Dong, L.; Sun, X.; et al. Estimating AVHRR snow cover fraction by coupling physical constraints into a deep learning framework. *ISPRS J. Photogramm. Remote Sens.* **2024**, *218*, 120–135. [CrossRef]
32. Zhu, L.; Zhang, Y.; Wang, J.; Tian, W.; Liu, Q.; Ma, G.; Kan, X.; Chu, Y. Downscaling Snow Depth Mapping by Fusion of Microwave and Optical Remote-Sensing Data Based on Deep Learning. *Remote Sens.* **2021**, *13*, 584. [CrossRef]
33. Gu, Q.; Xu, J.; Ni, J.; Peng, X.; Zhou, H.; Dong, L.; Yu, B.; Wu, J.; Zheng, Z.; Huang, Y. Improved snow depth estimation on the Tibetan Plateau using AMSR2 and ensemble learning models. *Int. J. Appl. Earth Obs. Geoinf.* **2024**, *133*, 104102. [CrossRef]
34. Vaswani, A.; Shazeer, N.; Parmar, N.; Uszkoreit, J.; Jones, L.; Gomez, A.N.; Kaiser, Ł.; Polosukhin, I. Attention is all you need. In Proceedings of the 31st International Conference on Neural Information Processing Systems, Long Beach, CA, USA, 4–9 December 2017; pp. 6000–6010.
35. Wang, W.; Chen, Z.; Chen, X.; Wu, J.; Zhu, X.; Zeng, G.; Luo, P.; Lu, T.; Zhou, J.; Qiao, Y.; et al. VisionLLM: Large Language Model is also an Open-Ended Decoder for Vision-Centric Tasks. In Proceedings of the 2023 Conference on Neural Information Processing Systems, New Orleans, LO, USA, 10–16 December 2023; pp. 61501–61513.
36. Ma, S.; Gao, X.; Jiang, L.; Xu, R. A Review of Visual Transformer Research. In Proceedings of the International Conference on Image, Vision and Intelligent Systems 2023 (ICIVIS 2023), Baoding, China, 16–18 August 2023; pp. 349–356.
37. Zhao, H. Long Time Series of Cloud-Free Fractional Snow Cover Products in China. Master's Thesis, Chinese Academy of Sciences, Beijing, China, 2020.
38. Hao, X.; Huang, G.; Che, T.; Ji, W.; Sun, X.; Zhao, Q.; Zhao, H.; Wang, J.; Li, H.; Yang, Q. The NIEER AVHRR snow cover extent product over China—A long-term daily snow record for regional climate research. *Earth Syst. Sci. Data* **2021**, *13*, 4711–4726. [CrossRef]
39. Brodzik, M.J.; Long, D.G.; Hardman, M.A. Best Practices in Crafting the Calibrated, Enhanced-Resolution Passive-Microwave EASE-Grid 2.0 Brightness Temperature Earth System Data Record. *Remote Sens.* **2018**, *10*, 1793. [CrossRef]
40. Meier, W.N.; Stewart, J.S. Assessing the Potential of Enhanced Resolution Gridded Passive Microwave Brightness Temperatures for Retrieval of Sea Ice Parameters. *Remote Sens.* **2020**, *12*, 2552. [CrossRef]
41. Cai, Y.; Duguay, C.R.; Ke, C.Q. A 41-year (1979–2019) passive-microwave-derived lake ice phenology data record of the Northern Hemisphere. *Earth Syst. Sci. Data* **2022**, *14*, 3329–3347. [CrossRef]
42. Liu, Y.; Yang, J.; Chen, X.; Yao, J.; Li, L.; Qiu, Y. Moderate-resolution snow depth product retrieval from passive microwave brightness data over Xinjiang using machine learning approach. *Int. J. Digit. Earth* **2024**, *17*, 2299208. [CrossRef]
43. Xiao, X.; Liang, S.; He, T.; Wu, D.; Pei, C.; Gong, J. Estimating fractional snow cover from passive microwave brightness temperature data using MODIS snow cover product over North America. *Cryosphere* **2021**, *15*, 835–861. [CrossRef]
44. Wei, Y.; Li, X.; Gu, L.; Zheng, X.; Jiang, T. A novel fine-resolution snow depth retrieval model to reveal detailed spatiotemporal patterns of snow cover in Northeast China. *Int. J. Digit. Earth* **2023**, *16*, 1164–1185. [CrossRef]
45. Berg, W.; Kroodsma, R.; Kummerow, C.D.; McKague, D.S. Fundamental Climate Data Records of Microwave Brightness Temperatures. *Remote Sens.* **2018**, *10*, 1306. [CrossRef]
46. Derksen, C.; LeDrew, E.; Walker, A.; Goodison, B. Influence of Sensor Overpass Time on Passive Microwave-Derived Snow Cover Parameters. *Remote Sens. Environ.* **2000**, *71*, 297–308. [CrossRef]
47. Wang, Y.; Huang, X.; Wang, J.; Zhou, M.; Liang, T. AMSR2 snow depth downscaling algorithm based on a multifactor approach over the Tibetan Plateau, China. *Remote Sens. Environ.* **2019**, *231*, 111268. [CrossRef]

48. Zhao, Q.; Hao, X.; Wang, J.; Sun, X.; Li, H. A dataset of snow phenology in China based on MODIS from 2000 to 2020. 2021. Available online: https://www.ncdc.ac.cn/portal/metadata/15157e5e-6c73-4d7e-91de-d769fef0a509 (accessed on 1 October 2023).
49. Mott, R.; Schirmer, M.; Bavay, M.; Grünewald, T.; Lehning, M. Understanding snow-transport processes shaping the mountain snow-cover. *Cryosphere* **2010**, *4*, 545–559. [CrossRef]
50. Che, T.; Dai, L. *Terrain Effects on Microwave Emission Transmission of Snowpack and Snow Depth Retrieval*; Copernicus Meetings: Göttingen, Germany, 2024.
51. Yang, J.W.; Jiang, L.M.; Lemmetyinen, J.; Pan, J.M.; Luojus, K.; Takala, M. Improving snow depth estimation by coupling HUT-optimized effective snow grain size parameters with the random forest approach. *Remote Sens. Environ.* **2021**, *264*, 112630. [CrossRef]
52. Xu, X.; Liu, X.; Li, X.; Shi, Q.; Chen, Y.; Ai, B. Global Snow Depth Retrieval From Passive Microwave Brightness Temperature With Machine Learning Approach. *IEEE Trans. Geosci. Remote Sens.* **2022**, *60*, 4302917. [CrossRef]
53. Wang, Y.; Zheng, Z. Representative evaluation dataset of snow cover observation space at CMA meteorological stations. Available online: https://www.ncdc.ac.cn/portal/metadata/5a08a130-baaf-432c-b39f-7651be08d263 (accessed on 1 April 2023).
54. Wang, J.; Che, T.; Li, Z.; Li, H.; Hao, X.; Zheng, Z.; Xiao, P.; Li, X.; Huang, X.; Zhong, X.; et al. Investigation on Snow Characteristics and Their Distribution in China. *Adv. Earth Sci.* **2018**, *33*, 12–26.
55. Chang, A.T.C.; Foster, J.L.; Hall, D.K.; Kelly, R.E.J.; Riggs, G.A. Assessment of the relative accuracy of hemispheric-scale snow-cover maps. *Ann. Glaciol.* **2002**, *34*, 24–30. [CrossRef]
56. Tao, C.; Liyun, D.; Xin, L. Long-term series of daily snow depth dataset in China (1979–2023). 2015. Available online: https://data.tpdc.ac.cn/en/data/df40346a-0202-4ed2-bb07-b65dfcda9368/ (accessed on 23 April 2023).
57. Yang, J.; Jiang, L.; Luojus, K.; Pan, J.; Lemmetyinen, J.; Takala, M.; Wu, S. Snow depth estimation and historical data reconstruction over China based on a random forest machine learning approach. *Cryosphere* **2020**, *14*, 1763–1778. [CrossRef]
58. Gorishniy, Y.; Rubachev, I.; Khrulkov, V.; Babenko, A. Revisiting Deep Learning Models for Tabular Data. In Proceedings of the 35th International Conference on Neural Information Processing Systems, NIPS'21, Online, 6–14 December 2021; pp. 18932–18943.
59. Devlin, J.; Chang, M.-W.; Lee, K.; Toutanova, K. BERT: Pre-training of Deep Bidirectional Transformers for Language Understanding. In Proceedings of the NAACL 2019, Minneapolis, MN, USA, 2–7 June 2019; pp. 4171–4186.
60. You, Y.; Li, J.; Reddi, S.J.; Hseu, J.; Kumar, S.; Bhojanapalli, S.; Song, X.; Demmel, J.; Keutzer, K.; Hsieh, C.-J. Large Batch Optimization for Deep Learning: Training BERT in 76 minutes. In Proceedings of the International Conference on Learning Representations, Addis Ababa, Ethiopia, 30 April 2020.
61. Loshchilov, I.; Hutter, F. SGDR: Stochastic Gradient Descent with Warm Restarts. In Proceedings of the International Conference on Learning Representations, Virtual, 25–29 April 2022.
62. Che, T.; Dai, L.; Zheng, X.; Li, X.; Zhao, K. Estimation of snow depth from passive microwave brightness temperature data in forest regions of northeast China. *Remote Sens. Environ.* **2016**, *183*, 334–349. [CrossRef]
63. Gao, S.; Li, Z.; Zhang, P.; Chen, Q.; Huang, L.; Zhou, J.; Zhao, C.; Qiao, H.; Zheng, Z. A novel global snow depth retrieval method considering snow metamorphism and forest influence. *Remote Sens. Environ.* **2023**, *295*, 113712. [CrossRef]
64. Jiang, L.; Shi, J.; Tjuatja, S.; Dozier, J.; Chen, K.; Zhang, L. A parameterized multiple-scattering model for microwave emission from dry snow. *Remote Sens. Environ.* **2007**, *111*, 357–366. [CrossRef]

Disclaimer/Publisher's Note: The statements, opinions and data contained in all publications are solely those of the individual author(s) and contributor(s) and not of MDPI and/or the editor(s). MDPI and/or the editor(s) disclaim responsibility for any injury to people or property resulting from any ideas, methods, instructions or products referred to in the content.